# Full-parameter performance simulation theory for velocity azimuth display pulsed coherent Doppler lidar, and error analysis on wind speed measurement in shear flow

Shumpei Kameyama[*1]

[1]*Mitsubishi Electric Corporation, Information Technology R&D Center, 5–1–1 Ofuna, Kamakura, Kanagawa, Japan 247–8501*

Full-parameter performance simulation theory is shown for velocity azimuth display pulsed coherent Doppler lidar (VAD-PCDL). The parameters include not only VAD-PCDL parameters but also atmospheric ones. Influences of these parameters regarding range-dependent intensity of heterodyne-detected signal and digital signal processing are considered. The simulation theory can be applied for general wind field cases. Example analysis of wind speed measurement error is shown for the case of sheared wind flow. Some cases of the vertical wind profiles with shear are set for the input, and wind speed measurement using VAD scan is performed using the fast Fourier transform (FFT) based signal processing. Approach of Monte-Carlo computer simulation is applied. With this method, we analyze the wind speed measurement error caused by factors of (i) shear curvature, (ii) signal-to-noise (SNR) weighting, and (iii) height sensing error.

**Key Words**: Coherent Doppler lidar, Wind speed measurement, Shear flow

## 1. Introduction

Recent growing of wind energy industry needs larger wind turbines with higher hub heights. Under this background, wind resource assessments at higher heights become more important in advance of wind farm constructions with large wind turbines. This causes the necessity of extremely tall meteorological masts for traditional wind resource assessments using cup anemometers. To prevent the above-mentioned necessity, a coherent Doppler lidar (CDL)[1–7] has been attractive since this device realizes remote wind sensing from the ground. Especially, the velocity azimuth display pulsed CDL (VAD-PCDL)[8, 9] provides vertical profiling of horizontal wind speed. A VAD-PCDL can be an alternative to a meteorological mast, even though it is still under discussed by the wind energy community if it can be a full replacement. The performances of VAD-PCDLs have been evaluated for the wind resource assessments in several measurement campaigns[8–15]. Further, activities on this application toward international standardization have been carried on, and some recommended practices have been published by the international energy agency (IEA) task[16, 17]. A VAD-PCDL is now a recognized device for wind resource assessments. However, there are some remaining issues toward wider application of wind resource assessments using VAD-PCDLs. One of the issues is understanding the influence of probe volume on wind measurement in inhomogeneous flow. A VAD-PCDL measures a weighted averaged wind speed within a probe volume even though a cup anemometer measures a wind speed at a certain point. This difference potentially causes measurement error for a VAD-PCDL if a wind speed at a certain point is defined as a true value. There are several kinds of inhomogeneous flow, for example, horizontal shear, wakes, and so on. Wind speed measurement errors of VAD-PCDLs with a set of fixed CDL parameters have been evaluated in several measurement campaigns under several wind flow conditions[8–15]. However, only few works have been performed for the influences of CDL parameters in these flows.

The influences of pulse shape (i.e., time profile of transmitting pulse energy of CDL) in wakes and horizontal shear have been studied[18, 19], but parameters which determine the range-dependent intensity of heterodyne-detected signal have not been considered. In addition, the influence of digital signal processing has not included in these works. For VAD-PCDLs, several parameters (for example, beam focusing distance, atmospheric transmittance, etc.) impact the range-dependent intensity of heterodyne-detected signal. Further, parameters for digital signal processing (time gate width, line-of-sight (LOS) wind velocity estimation algorithm, etc.) impact wind speed measurement accuracy. Therefore, simulation method for error analysis using more detailed model has been necessary for the understanding of VAD-PCDL measurement.

In this paper, the performance simulation theory with full VAD-PCDL parameters is shown. Example analysis of wind speed measurement error is shown for the case of sheared wind flow. Although the influence of pulse shape has been considered in complex flow (i.e., wakes)[19], simpler wind flow of horizontal shear is assumed here. The under-standing of measurement error in shear flow is very important, since it is one of representative and the most basic wind field in wind resource assessments.

In the simulation of this paper, the model of the received signal (heterodyne-detected signal of a PCDL) is expressed as the summation of incoherent backscattered signals from the thin sliced atmospheric ranges and detector noise. The speckle effect, which is a feature of a PCDL signal, can be modelled by the above-mentioned summation. The intensity of the received signal from each sliced range is weighted using the signal to noise ratio (SNR) equation. Full PCDL parameters, including the pulse shape, range resolution, and focal range of laser beam, are considered in the simulation. The atmospheric conditions, including the atmospheric transmission, backscatter coefficient, and wind profile, are also considered. Some cases of the vertical wind profiles with shear are set for the input. Ideal horizontal wind profiles with vertical shear are assumed. Wind speed measurement using VAD scan is simulated using the fast Fourier transform (FFT) based signal processing in the Monte-Carlo method. Using this simulation, we analyze the wind speed measurement error caused by factors of (i) shear curvature, (ii) SNR weighting, and (iii) height sensing error.

The rest of this paper is organized as follows. Basic configuration and operation of a VAD-PCDL are shown in section 2. Model of heterodyne-detected signal is described in section 3. Simulation procedure for error analysis is explained in section 4. Error sources are shown in section 5. Simulation parameters and results with some investigations are introduced in section 6 and 7. Comparison with past work is shortly investigated in section 8. Some parts of this paper have been presented in the 18th international symposium for advancement of boundary-layer remote sensing (ISARS) in 2016, but the proceedings had not been published because of unknown reasons. Minor differences exist regarding the simulation results between the previous presentation and this paper because of some correction on the detailed simulation. Further, detail explanations and new simulation results are newly shown in this paper.

## 2. VAD-PCDL

The configuration of a VAD-PCDL is schematically shown in Fig. 1. The detail of each component is not explained here since this is outside the scope of this paper (for more detail, see an example[7]). A continuous wave laser light is transmitted and divided. A part of the divided light is sent to a balanced receiver as a local light. The other part is pulse modulated, amplified, and transmitted to the atmosphere through an optics. The backscattered light from aerosols in the atmosphere is received through the same optics and a circulator. The received light is heterodyne-detected with the local light by the balanced receiver. The heterodyne-detected signal is analogue-to-digital (A/D) converted and is processed by a signal processor, and a range dependence of line-of-sight wind velocity is estimated using range gating and spectral analysis using FFT and incoherent spectrum accumulation. The LOS wind velocity is estimated as the first moment of the spectrum, which is given by

$$V_{LOS} = \frac{\lambda}{2MT_S} \left( \frac{\sum_{i=p-w}^{p+w} [(i-p) \cdot S(i)]}{\sum_{i=p-w}^{p+w} S(i)} \right), \qquad (1)$$

where $\lambda$ is the laser wavelength (m), $M$ is the sample number in a range gate, $T_S$ is the sampling interval, $S(i)$ is the spectrum obtained by FFT (a.u.), $i$ is the frequency bin number, $p$ is the peak frequency bin, and $w$ is the width used for the first-moment operation. The FFT-based LOS wind velocity estimation with the above-mentioned moment operation
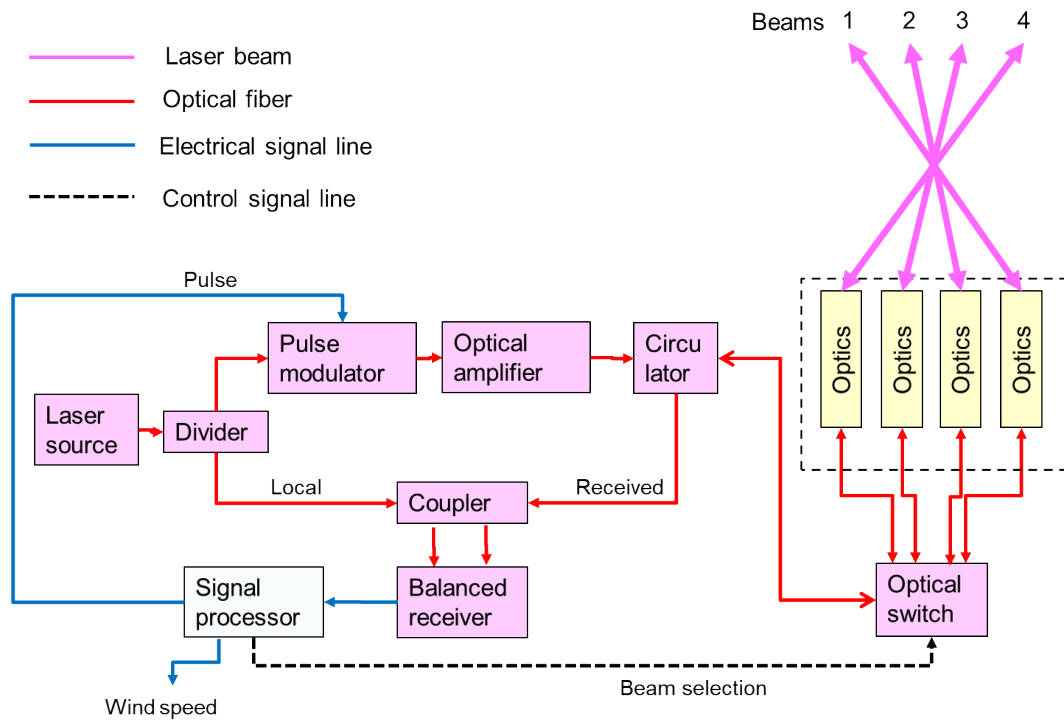
Fig. 1  Schematic of VAD-PCDL configuration.
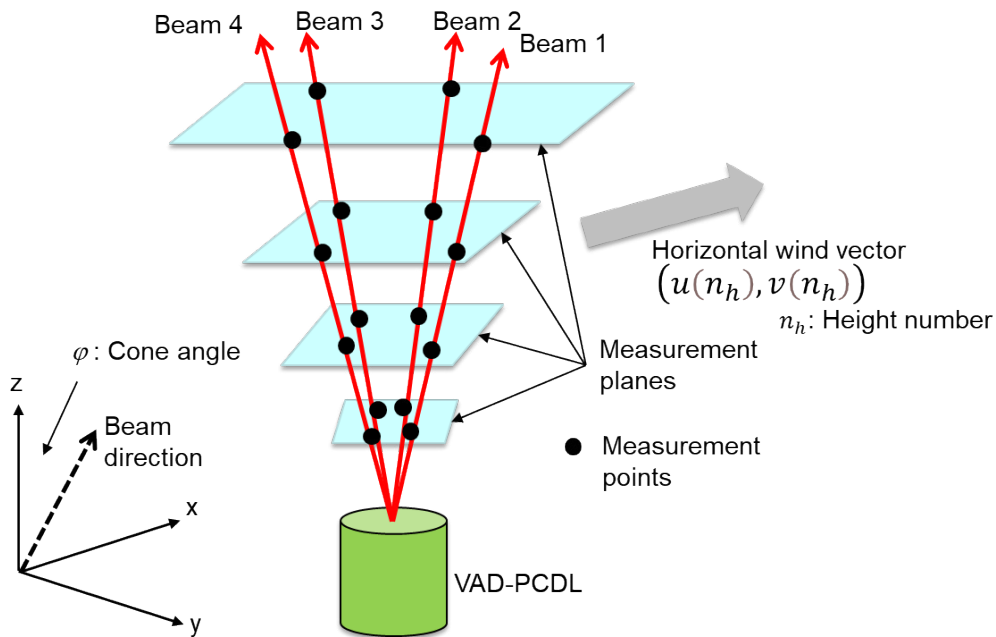


Fig. 2  Schematic of VAD measurement.

is influenced by shear flow or turbulence within a probe volume. However, this estimation method is an authentic one for processing of weather echoes[20], and it is widely used for the existing CDLs[9, 10] because of the merit of real-time processing and the high signal detection ability.

The VAD-PCDL in the figure has four beams with 90 degrees interval for circumferential direction. The above-mentioned configuration with fiber-based circuit is basically same as the ones in[6, 7, 9]. The line-of-sight (LOS) wind velocity is obtained for each beam with changing selected beam (from 1 to 4).

The schematic of wind speed measurement for a VAD-PCDL is shown in Fig. 2. Wind speed vector at a certain

height (($u(n_h)$, $v(n_h)$), $n_h$: height number of range gates) are obtained by assuming homogeneous wind field as[9, 15]

$$u(n_h) = \frac{V_{L2}(n_h) - V_{L4}(n_h)}{2 \sin \varphi}, \qquad (2)$$

$$v(n_h) = \frac{V_{L1}(n_h) - V_{L3}(n_h)}{2 \sin \varphi}, \qquad (3)$$

where $V_{Lb}(n_h)$ is the LOS velocity (m/s) of the beam number $b$ ( = 1, 2, 3, 4), and $\varphi$ is the cone angle (rad). The vertical wind component can be obtained using velocities of the beam 1,3 or 2,4 but is not considered here.

The horizontal wind speed and direction are calculated by[9, 15]

$$V_h(n_h) = \sqrt{u(n_h)^2 + v(n_h)^2}, \qquad (4)$$

$$\theta_h(n_h) = tan^{-1} \frac{v(n_h)}{u(n_h)}. \qquad (5)$$

## 3. Model of heterodyne-detected signal

Here, a heterodyne-detected signal is expressed as the summation of incoherent backscattered signals from sliced atmospheric ranges and detector noise. This model is denoted in Fig. 3. The model of a heterodyne-detected signal is the one which has been denoted in past literatures[21, 22], and it is combined with the SNR equation[23, 24]. The validity of the signal model has been confirmed in comparison with actual CDL data[21]. The SNR equation has been evaluated experimentally in the past[6, 22]. In general, a heterodyne-detected signal with an intermediate frequency and complex time samples are generated using an in-phase quadrature (IQ) detector and two channel A/D converters. Consequently, the signal in the digital domain is expressed as[22]

$$
\begin{aligned}
S(m, i_{IT}) = & \sqrt{\frac{2\sqrt{ln\,2}\,T_S}{\sqrt{\pi}\Delta t}} \\
& \cdot \sum_{\tau=0}^{P} \left\{ x(\tau, i_{IT}) \exp\left\{ j\left[ \frac{4\pi V_L(\tau)}{\lambda}(m-1)T_S \right] \right\} \times \exp\left( -2\,ln\,2 \cdot \frac{(m \cdot T_S - 2\tau\Delta L/c)^2}{\Delta t^2} \right) \cdot \sqrt{SNR(\tau)} \right\} \\
& + N_{oise}(m, i_{IT}), \qquad (6)
\end{aligned}
$$

where $m$ denotes the sample number corresponding to the time; $i_{IT}$, the iteration number in the Monte-Carlo simulations; $\tau$, the sliced atmospheric range number; $\Delta t$, the Full Width Half Maximum (FWHM) of the transmitting pulse (s) ; $\Delta L$, the length of the sliced atmospheric range; and $c$, the speed of light (m/s). SNR ($\tau$) denotes the SNR at range number $\tau$, which is the signal-to-noise ratio of the average signal power to the average noise power. $N_{oise}(m, i)$ denotes the complex amplitude of the white Gaussian detector noise having normalized average power of 1, and $x(\tau, i)$ denotes the complex amplitude of the signal from each atmospheric range and the complex statistically independent zero mean Gaussian variable with normalized average power of 1. This statistical property expresses the speckle effect of the signals. $V_L(\tau)$ denotes the line-of-sight (LOS) wind velocity of each sliced range (m/s) which corresponds to the assumed wind field. In the cases of a VAD-PCDL and ideal horizontal wind field (zero vertical wind), the LOS velocity is obtained by the projection of the horizontal wind speed to the LOS direction. $P$ is the number of the sliced atmospheric ranges considered in the simulation should be considerably larger than the simulated range region. It is assumed that the SNR is constant in the above-mentioned atmospheric slices ranges and the spectrum of the transmitting pulse is the Fourier transform limit. It should be noted that only envelopes (i.e., intensity profiles) of signals from the sliced atmospheric ranges are shown in Fig. 3, but the summation of these signals is performed in complex (i.e., electrical field) domain. This point is expressed in eq. (6).

The SNR, which is proportional to the range-dependent intensity of heterodyne-detected signal, determines the range-dependent weighting of the signal in eq. (6), and is expressed as[24]
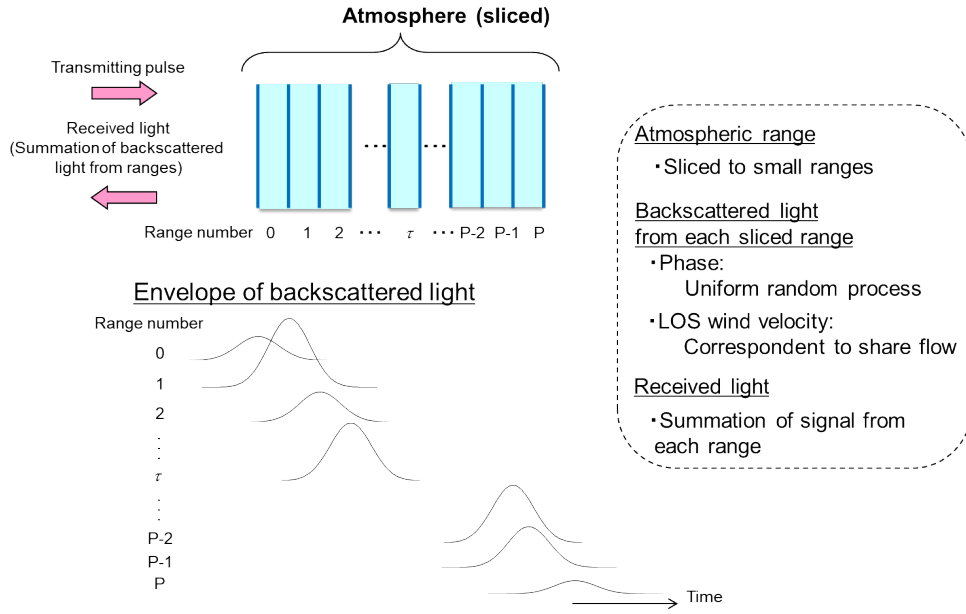
Fig. 3 Schematic of signal from sliced atmospheric ranges. Each sliced range has a wind speed corresponding to a wind field.

$$SNR(\tau) = \frac{\eta_D(L)\lambda E\beta K^{2L/1000}\pi D^2}{8hBL^2}, \qquad (7)$$

where $h$ is Planck's constant (Js), $E$ is the transmitting pulse energy (J), $D$ is the receiving aperture diameter (m), $L$ is the range (m) ($=\tau\Delta L$), which is given by $L = z/\cos\varphi$, where $z$ is the height (m). $B$ is the receiver bandwidth (Hz), $\beta$ is the atmospheric backscatter coefficient (m$^{-1}$ sr$^{-1}$), and $K$ is the atmospheric transmittance (km$^{-1}$). $\eta_D$ is the system efficiency given by[24]

$$\eta_D(L) = \frac{\eta_F}{\left\{1 + \left(1 - \frac{L}{L_F}\right)^2 \left[\frac{\pi(A_C D)^2}{4\lambda L}\right]^2 + \left(\frac{A_C D}{2S_0(L)}\right)^2\right\}}, \qquad (8)$$

where $A_C$ is the correction factor, and the approximated diameter of the transmitting beam is $A_c D$[24]. $\eta_F$ is the far-field system efficiency. $S_0(L)$ is the transverse coherent length (m), and if the refractive index structure constant ($C_n^2$(m$^{-2/3}$)) is constant along the beam path, $S_0(L)$ is approximated by $(1.1k^2 L C_n^2)^{-3/5}$ where $k$ is the wave number ($=2\pi/\lambda$). $L_F$ is the focal range of the transmitting beam (m). In cases of VAD-PCDL, this parameter is given by $L_F = L_h/cos\varphi$, where $L_h$ is the beam focusing height (m). The equations (7) and (8) show that the range dependence of SNR weighting is expressed by complex combination of several terms. These are (i) optical attenuation in the atmosphere (in numerator of eq. (7), which is caused by optical extinction and absorption), (ii) diffuse attenuation regarding aerosol scattering ($L^2$ in denominator of eq. (7)), (iii) beam focusing effect (in second term of denominator of eq. (8)), (iv) aberration caused by refractive turbulence (in third term of denominator of eq. (8)), and (v) receiving aperture diameter (in second and third term of denominator in eq. (8)).

The wind field is assumed to be ideal horizontal wind and has the simple power low formulation as[18]

$$U(z) = U_0\left(\frac{z}{z_0}\right)^\alpha, \qquad (9)$$

where $z_0$ is the reference height (m), $U_0$ is the reference speed (m/s)which is set as a deterministic value, and $\alpha$ is the shear exponent of the horizontal wind speed. The LOS velocity in eq. (6) can be obtained using this equation and the cone angle in the VAD measurement. Several shear behaviors can appear under different atmospheric stability conditions. However, the assumption of eq. (9) is suitable for the basis of understanding and this expression has been used in several wind field analysis[25, 26]. The simulation for other shear models can be possible by simply substituting the wind field instead of eq. (9).

## 4. Simulation procedure

Schematic of simulation procedure is shown in Fig. 4. Since the signal model of eq. (6) includes the random process, the Monte-Carlo simulation is used. The parameters which has the random process in eq. (6) are $x(\tau, i)$, SNR$(\tau)$, and $N_{oise}$ $(m, i)$. A heterodyne-detected signal is generated by a computer, according to (6) and the random process described in section 3. Then, the signal is range-gated, and signal processing and velocity estimation are performed according to the algorithm corresponding to the selected velocity estimator. The schematic of the simulated heterodyne-detected signal and signal processing is denoted in Fig. 5. In the figure, $N$ is the range gate number for the signal processing corresponding to the wind sensing ranges (which is different from the sliced atmospheric range number: $\tau$). Following the
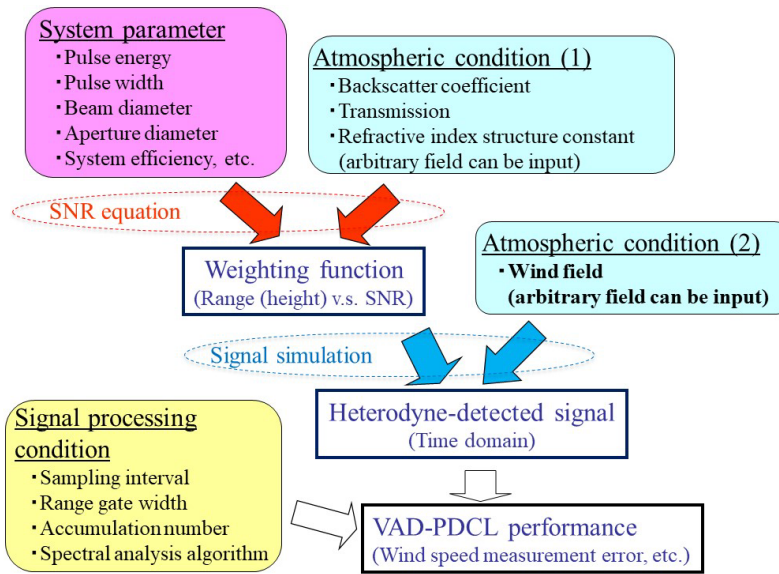
Fig. 4    Schematic of simulation procedure.
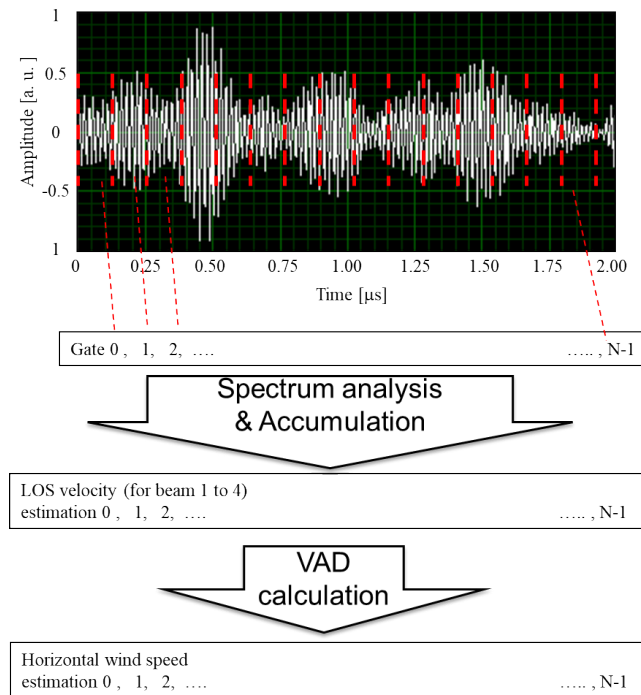
Fig. 5    Schematic of the simulated heterodyne-detected signal and signal processing.

iterations of this simulation procedure, the periodogram (i.e. spectrum) is accumulated and the LOS velocity is obtained using the pre-determined method. The four direction (90 degrees interval) VAD is considered. The wind direction is assumed to be constant regarding its height profile and also to be the same as the horizontally projected vector of the two of the beams.

## 5. Error sources

Basically, wind speed measurement error for VAD-PCDL is caused by asymmetry regarding wind profile and/or SNR weighting within a probe volume. The following three factors are considered. These are schematically shown in Fig. 6.

- Shear curvature (Fig. 6(a)) : The error caused by this factor is expressed as '$\Delta_C$' and given in per cent ( $= (U_l - U_t)/U_t \cdot 100$) where $U_l$ is the horizontal wind speed measured by a VAD-PCDL and $U_t$ is the true horizontal wind speed at the nominal height which is given by eq. (6).

- SNR weighting (Fig. 6(b)) : This error is caused by the combined effect of the shear curvature and the SNR weighting. This is expressed as '$\Delta_S$' and also given in percent. In general, the weighting has a peak value around the beam focusing height and decreases for other height region owing to the defocusing characteristic of eq. (7) and (8). For larger heights, the decreasing is more distinct owing to many sources (optical attenuation in the atmosphere, etc.).

- Height sensing error (Fig. 6(c)) : This error is caused by the combined effect of the shear curvature, the SNR weighting, and ＋0.65 m of sensing height error (i.e., sensing at 80.65 m instead of 80 m). The value of 0.65 m corresponds to one sampling interval in Table 2 which is projected from LOS to height direction. This is expressed
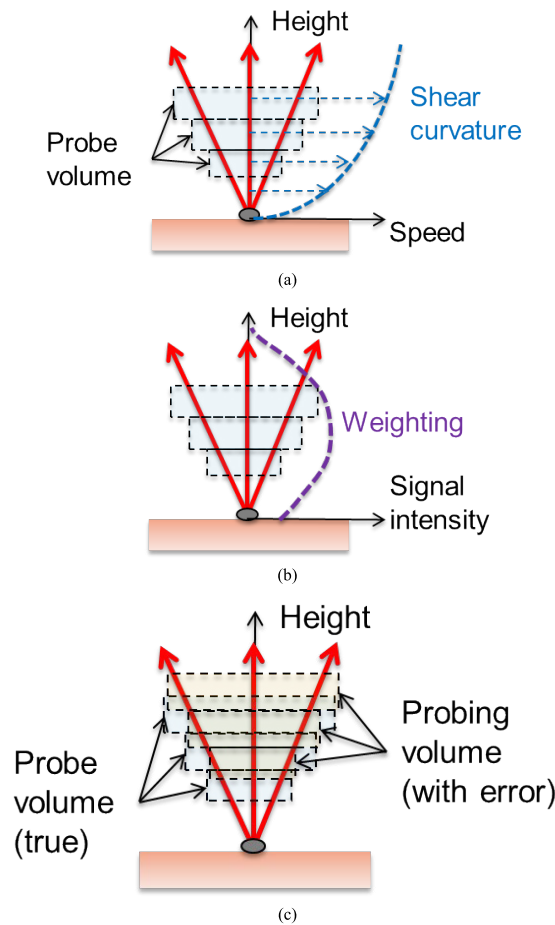


Fig. 6　Schematic of (a) : shear curvature, (b) SNR weighting, and (c) : height sensing error.

Table 1　Factors which are considered in three kinds of errors.

| Factor ＼ Symbol | $\Delta_C$ | $\Delta_S$ | $\Delta_H$ |
|---|---|---|---|
| Shear curvature | ○ | ○ | ○ |
| SNR weighting | × | ○ | ○ |
| Height sensing error | × | × | ○ |

as '$\Delta_H$' and also given in percent.

Factors which are considered in the above-mentioned three errors ($\Delta_C$, $\Delta_S$, and $\Delta_H$) are shown in Table 1.

## 6. Simulation condition

Simulation parameters are shown in Table 2. Simulations are performed for five shear exponent cases. The range of shear exponent has been set by referencing a past literature[18]. The value of FWHM of the transmitting pulse corresponds to probe length of 20 m. The beam focusing heights of 100 m and 200 m correspond to the focal ranges of transmitting beam of 230.94 m and 115.47 m by considering the beam cone angle. Two receiving aperture diameters of 0.04 m and 0.07 m are considered. The cone angle of $\pi/6$ rad ($=30$ degrees) is assumed. The above-mentioned instrumental parameters are set by referencing existing PCDLs[6, 7, 9]. The above-mentioned variety of parameters causes changes of weighting function (i.e., height dependence of SNR). The height profiles of horizontal wind speed, pulse weighting, and SNR weighting are shown in Fig. 7. The pulse weighting is the same as the pulse shape, and it is projected to the height direction in the figure. This weighting corresponds to volume averaging effect for LOS (or height) direction and

Table 2　Simulation parameters.

| Parameter | | Value | Unit | Symbol |
|---|---|---|---|---|
| Physical parameters | Planck's constant | - | Js | $h$ |
| | Speed of light | - | m/s | $c$ |
| Atmospheric parameters | Atmospheric backscatter coefficient | - | /m/sr | $\beta$ |
| | Atmospheric transmittance | 0.90 | /km | $K$ |
| | Atmospheric refractive index structure constant | 0 | $m^{-2/3}$ | $C_n^2$ |
| Wind condition | Reference height | 80.00 | m | $z_0$ |
| | Reference speed | 10.00 | m/s | $U_0$ |
| | Shear exponent | 0.0, 0.1, 0.2, 0.3 | | $\alpha$ |
| Instrumental parameters | Laser wavelength | $1.55 \times 10^{-6}$ | m | $\lambda$ |
| | Transmitting pulse energy | - | J | $E$ |
| | FWHM of the transmitting pulse | $1.56 \times 10^{-7}$ | s | $\Delta t$ |
| | Receiving aperture diameter | 0.04, 0.07 | m | $D$ |
| | Correction factor | 0.71 | - | $A_C$ |
| | Beam focusing height | 100, 200 | m | $L_h$ |
| | Receiver bandwidth | - | Hz | $B$ |
| | Beam cone angle | $\pi/6$ | rad | $\varphi$ |
| Signal processing parameters | Sampling interval | $5 \times 10^{-9}$ | s | $T_S$ |
| | Frequency bin width for moment operation | 5 | - | $w$ |
| | Sample number in a range gate | 32 | - | $M$ |
| Simulation parameters | Spectral accumulation number | 50,000 | - | - |
| | Length of the sliced atmospheric range | 0.025 | m | $\Delta L$ |
| | Number of the sliced atmospheric ranges | 16,000 | - | $P$ |
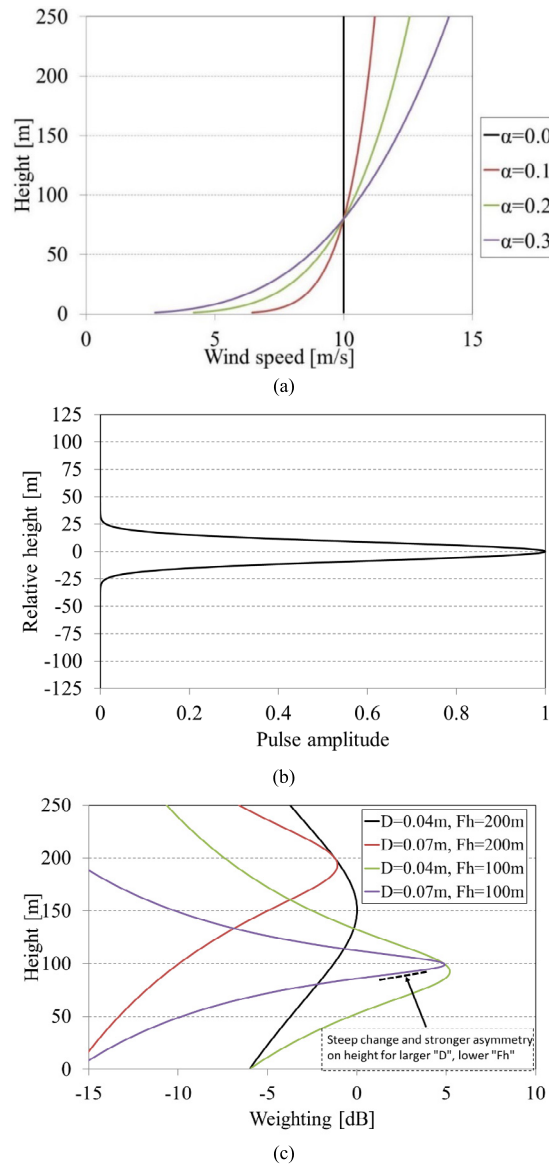
Fig. 7    Height profiles of (a) : Horizontal wind speed, (b) : Pulse weighting, and (c) : SNR weighting. The weighting in (c) is normalized by the maximum value for the case of D = 0.04 m and Fh = 200 m. Tendency on SNR weighting on height is schematically explained in (c).

becomes an error source in wind speed measurement. In some cases (for example, in the case of $D = 0.04$ m and $F_h =$ 200 m), SNR weighting does not become maximum at a beam focusing height. This situation tends to appear when the approximated diameter of the transmitting beam (i.e., $A_c D$ in eq. (8), which is proportional to $D$), is small. In such a case, the beam focusing effect is weak and the range-dependent SNR attenuation in eq. (7) overcomes the beam focusing effect in eq. (8). In general, steep change and stronger asymmetry of SNR weighting appears on height profile for larger $D$ and lower $F_h$. This is known from eq. (8), and can be seen in Fig. 7(c).

The sampling interval of 5 ns corresponds to the LOS length of 0.75 m. The length of sliced atmospheric range of 0.025 m is set smaller than the sampling interval. The set of sampling interval and sampling number in a range gate determines a range gate width, and it corresponds to the width of 21 m by projection to height direction. FFT is chosen as a velocity estimator. The LOS velocity is obtained from the first moment of the peak in the spectrum which is calculated using FFT. The spectral accumulation number of 50,000 is performed to reduce speckle noise.

The instrumental parameters in Table 2 are just examples. Further discussion is needed for the general case. Further,

the detector noise is neglected in the simulation of this paper to reduce the influence of random noise. Therefore, some of the parameters, of which the contribution to SNR is simply proportional (for example, atmospheric backscatter coefficient, transmitting pulse energy, etc.), do not impact the simulation results. The values of these parameters are not denoted in the table. The value of the correction factor is the optimum one for the given diameter of the circular receiving aperture. This corresponds to the case that the $1/e^2$ intensity beam diameter is 80% of the diameter of the aperture.

## 7. Simulation results

The simulation results regarding the cases in Table 2 and Fig. 7 are shown in tables 3 to 6. True wind speed for each height and each case of shear exponent is additionally shown in the tables. It should be noted that the errors in the tables are relative values in unit of "%" (not "m/s"). If the error values in unit of "m/s" are same for multiple heights, the

Table 3　Results of error analysis ($D = 40$ mm, $F_h = 200$ m).

| Shear exponent: $\alpha$ | Height (m) | $\Delta_C$ (%) | $\Delta_S$ (%) | $\Delta_H$ (%) | $U_t$ (m/s) |
|---|---|---|---|---|---|
| 0.0 | 40 | -0.1 | -0.1 | 0.1 | 10.000 |
| | 80 | 0.1 | 0.0 | 0.0 | 10.000 |
| | 120 | 0.0 | 0.1 | -0.1 | 10.000 |
| | 150 | 0.2 | 0.1 | 0.1 | 10.000 |
| | 200 | 0.0 | 0.0 | 0.0 | 10.000 |
| 0.1 | 40 | 0.0 | 0.2 | 0.3 | 9.330 |
| | 80 | -0.1 | -0.1 | 0.1 | 10.000 |
| | 120 | 0.1 | 0.1 | 0.1 | 10.414 |
| | 150 | -0.1 | 0.0 | 0.1 | 10.649 |
| | 200 | -0.1 | -0.2 | 0.0 | 10.960 |
| 0.2 | 40 | -0.1 | 0.3 | 0.5 | 8.706 |
| | 80 | 0.0 | 0.2 | 0.6 | 10.000 |
| | 120 | 0.0 | 0.3 | 0.3 | 10.844 |
| | 150 | -0.1 | 0.1 | 0.3 | 11.340 |
| | 200 | -0.1 | 0.0 | 0.0 | 12.011 |
| 0.3 | 40 | 0.2 | 0.4 | 0.5 | 8.122 |
| | 80 | 0.0 | 0.2 | 0.5 | 10.000 |
| | 120 | 0.1 | 0.3 | 0.3 | 11.293 |
| | 150 | -0.1 | 0.2 | 0.3 | 12.075 |
| | 200 | 0.0 | -0.1 | 0.0 | 13.163 |

Table 4　Results of error analysis ($D = 40$ mm, $F_h = 100$ m).

| Shear exponent: $\alpha$ | Height (m) | $\Delta_C$ (%) | $\Delta_S$ (%) | $\Delta_H$ (%) | $U_t$ (m/s) |
|---|---|---|---|---|---|
| 0.0 | 40 | -0.1 | 0.2 | -0.1 | 10.000 |
| | 80 | 0.1 | -0.1 | -0.1 | 10.000 |
| | 120 | -0.2 | 0.2 | 0.1 | 10.000 |
| | 150 | 0.1 | -0.1 | -0.1 | 10.000 |
| | 200 | -0.2 | -0.1 | -0.1 | 10.000 |
| 0.1 | 40 | -0.2 | 0.3 | 0.3 | 9.330 |
| | 80 | 0.0 | 0.4 | 0.6 | 10.000 |
| | 120 | -0.2 | -0.2 | -0.4 | 10.414 |
| | 150 | 0.0 | -0.2 | 0.0 | 10.649 |
| | 200 | -0.1 | 0.0 | 0.1 | 10.960 |
| 0.2 | 40 | -0.2 | 0.6 | 1.0 | 8.706 |
| | 80 | 0.1 | 0.8 | 1.0 | 10.000 |
| | 120 | 0.1 | -0.6 | -0.7 | 10.844 |
| | 150 | -0.1 | -0.2 | -0.2 | 11.340 |
| | 200 | -0.1 | 0.0 | -0.1 | 12.011 |
| 0.3 | 40 | -0.1 | 0.7 | 1.6 | 8.122 |
| | 80 | 0.0 | 1.4 | 1.6 | 10.000 |
| | 120 | 0.1 | -1.0 | -0.6 | 11.293 |
| | 150 | 0.1 | -0.4 | -0.1 | 12.075 |
| | 200 | -0.1 | -0.1 | -0.1 | 13.163 |

Table 5　Results of error analysis ($D$ = 70 mm, $F_h$ = 200 m).

| Shear exponent: $\alpha$ | Height (m) | $\Delta_C$ (%) | $\Delta_S$ (%) | $\Delta_H$ (%) | $U_t$ (m/s) |
|---|---|---|---|---|---|
| 0.0 | 40 | 0.0 | -0.1 | 0.0 | 10.000 |
|  | 80 | -0.1 | -0.1 | -0.1 | 10.000 |
|  | 120 | 0.1 | 0.2 | 0.1 | 10.000 |
|  | 150 | -0.1 | -0.2 | -0.1 | 10.000 |
|  | 200 | -0.1 | 0.0 | 0.0 | 10.000 |
| 0.1 | 40 | 0.0 | 0.0 | 0.2 | 9.330 |
|  | 80 | 0.2 | 0.2 | 0.2 | 10.000 |
|  | 120 | 0.0 | 0.2 | 0.3 | 10.414 |
|  | 150 | 0.2 | -0.1 | 0.0 | 10.649 |
|  | 200 | 0.0 | -0.1 | 0.0 | 10.960 |
| 0.2 | 40 | 0.0 | 0.2 | 0.5 | 8.706 |
|  | 80 | 0.0 | -0.1 | 0.3 | 10.000 |
|  | 120 | 0.2 | 0.2 | 0.3 | 10.844 |
|  | 150 | 0.0 | 0.2 | 0.5 | 11.340 |
|  | 200 | 0.1 | -0.1 | 0.0 | 12.011 |
| 0.3 | 40 | 0.0 | 0.5 | 0.9 | 8.122 |
|  | 80 | 0.1 | 0.3 | 0.4 | 10.000 |
|  | 120 | 0.1 | 0.4 | 0.4 | 11.293 |
|  | 150 | 0.0 | 0.4 | 0.4 | 12.075 |
|  | 200 | -0.1 | -0.1 | -0.1 | 13.163 |

Table 6　Results of error analysis ($D$ = 70 mm, $F_h$ = 100 m).

| Shear exponent: $\alpha$ | Height (m) | $\Delta_C$ (%) | $\Delta_S$ (%) | $\Delta_H$ (%) | $U_t$ (m/s) |
|---|---|---|---|---|---|
| 0.0 | 40 | 0.0 | -0.1 | 0.0 | 10.000 |
|  | 80 | 0.1 | 0.0 | 0.1 | 10.000 |
|  | 120 | -0.1 | -0.1 | 0.0 | 10.000 |
|  | 150 | 0.1 | -0.1 | -0.1 | 10.000 |
|  | 200 | 0.1 | -0.1 | -0.2 | 10.000 |
| 0.1 | 40 | -0.2 | 0.2 | 0.4 | 9.330 |
|  | 80 | 0.1 | 0.8 | 0.7 | 10.000 |
|  | 120 | 0.1 | -0.6 | -0.6 | 10.414 |
|  | 150 | 0.0 | -0.1 | 0.0 | 10.649 |
|  | 200 | -0.1 | -0.2 | -0.2 | 10.960 |
| 0.2 | 40 | 0.0 | 0.5 | 1.0 | 8.706 |
|  | 80 | -0.1 | 1.6 | 1.6 | 10.000 |
|  | 120 | 0.0 | -0.8 | -1.0 | 10.844 |
|  | 150 | -0.1 | -0.2 | -0.1 | 11.340 |
|  | 200 | 0.0 | -0.1 | -0.2 | 12.011 |
| 0.3 | 40 | 0.2 | 1.0 | 1.6 | 8.122 |
|  | 80 | 0.1 | 2.3 | 2.4 | 10.000 |
|  | 120 | -0.1 | -1.2 | -1.3 | 11.293 |
|  | 150 | 0.2 | -0.3 | -0.2 | 12.075 |
|  | 200 | -0.1 | 0.0 | 0.0 | 13.163 |

error values in the tables tend to become larger for lower heights, since the true wind speeds have smaller values for lower heights (see, eq. (9) and the values of $U_t$ in tables 3 to 6). The NORSEWInD standard stated the acceptance criteria of lidar performance for wind resource assessments, and the acceptance criteria for a linear regression slope between 0.98 and 1.01 has been stated[14]. This corresponds to $-2\%$ to $+1\%$ error, and these values are references for investigation on the values in the tables. Basically, the error becomes larger when the change of wind speed or the SNR weighting are steep and asymmetric. To clarify this tendency, representative values in the tables are plotted in Figs. 8 to 10. Figure 8 shows the comparison of height profiles of the three errors (caused by shear curvature, SNR weighting, and height sensing error) in the case of the receiving aperture diameter of 0.04 m and the beam focusing height of 100 m. The error caused by shear curvature is not so distinct compared with other error sources, but the error considering SNR weighting and height sensing error are more than $+1\%$ around the beam focusing height because of the steep change of
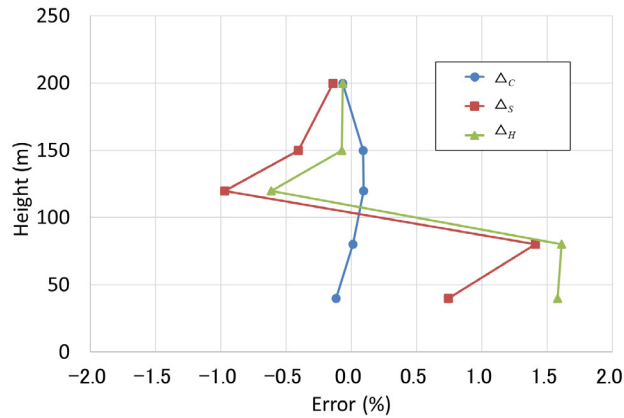
Fig. 8　Height profile of each error ($D = 0.04$ m, $F_h = 100$ m, $\alpha = 0.3$).
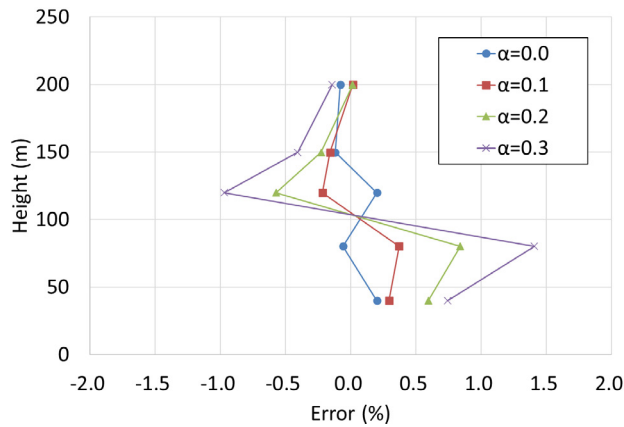


Fig. 9　Height profile of error caused by SNR weighting ($\Delta_S$) for each shear exponent ($D = 0.04$ m, $F_h = 100$ m).
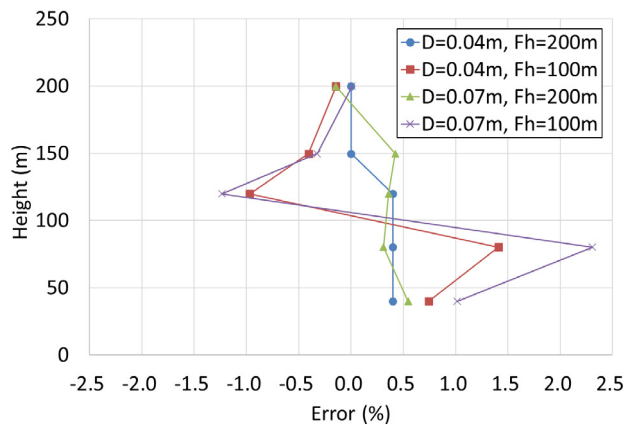


Fig. 10　Height profile of error caused by SNR weighting ($\Delta_S$) for each condition of receiving aperture diameter and focal height ($\alpha = 0.3$).

weighting at the region. It is known that the SNR weighting and heigh sensing error should be taken care of in wind resource assessment. Figure 9 shows the height profile of error $\Delta_S$ (caused by SNR weighting) for each shear exponent for the case of same value of the receiving aperture diameter and the beam focusing height in Fig. 8. The error becomes larger for the larger values of shear exponent $\alpha$ and exceeds ＋1% in the case of $\alpha = 0.3$ which is a realistic shear flow at the field for wind energy[18]. Figure 10 shows height profile of $\Delta_S$ regarding each condition of the receiving aperture diameter and the beam focusing height in the case of the above-mentioned realistic shear flow (i.e., $\alpha = 0.3$). The larger

receiving aperture diameter and the lower beam focusing height realize the higher SNR at the beam focusing height (see, Fig. 7(c)). The higher SNR contributes to high data availability which is outside the scope of this paper but important term in wind resource assessment[9]. However, the above-mentioned situations (larger receiving aperture diameter and/or lower beam focusing height) cause steeper change and stronger asymmetry on SNR weighting around the beam focusing height (see eq. (8) and Fig. 7(c)). Therefore, the error $\Delta_S$ caused by SNR weighting and $\Delta_H$ caused by height sensing error become larger for these cases. Totally, the error is determined quantitively by the combination of the above-mentioned tendencies. Parameters of VAD-PCDL (especially, the receiving aperture diameter and the beam focusing height) should be optimized by considering requirements regarding wind speed measurement accuracy and data availability in wind resource assessment. This optimization can be realized by understanding the error sources ($\Delta_C$, $\Delta_S$, and $\Delta_H$) quantitively and independently. For example, if $\Delta_S$ is the dominant factor in the error, the beam focusing effect should be reduced by tuning the receiving aperture diameter or the beam focusing height. If, only $\Delta_H$ is dominant, the sampling interval of A/D converter should be shorter. If $\Delta_C$ is dominant, this means the error source is the wind field itself. In such a case, making pulse width shorter for higher range resolution might be effective. This reduces the volume averaging effect along with LOS direction, even though the shorter pulse causes spectral broadening and negative influence on the accuracy of wind speed measurement. This influence should be paid attention.

In the tables, the three errors become small and theoretically should be zero for the cases of $\alpha = 0$, since wind speed uniformly distributes in this case. There are contradictions with the values lower than or equal to 0.2% which do not correspond to the above-mentioned theory. The error of 0.2% is not negligible by considering the acceptance criteria (wind speed measurement accuracy of 1%) in wind resource assessment[14]. The reason of the contradictions should be investigated further, but this may be caused by the limited iteration number of the Monte-Carlo simulation (i.e., 16,000) or the thickness of sliced atmosphere. Also, there is a possibility that the signal processing algorithm (i.e. FFT-based, here) is the source of this irregularities. The interval of Doppler velocity bin in the spectrum, which is determined by the wavelength, sampling interval, and the sample number in the range gate, is 4.84 m/s. On the other hand, the wind speed at the reference height of 80 m is 10 m/s, and the error corresponding to 0.2% error is 0.02 m/s (see Fig. 11). This error corresponds to the 1/242 (very small) of the velocity bin interval. Therefore, it is not easy to realize this velocity estimation accuracy, even though the spectral moment estimation of eq. (1) could realize the accurate estimation with 0.2% as shown in tables 3–6. Some additional processing (for example, zero-padding[27]) has potential to reduce the error. However, the simple FFT-based method has been employed here since this method has an advantage regarding the real-time processing. The effect of the above-mentioned additional processing can be simulated easily by adopting the processing to the simulated heterodyne-detected signals.
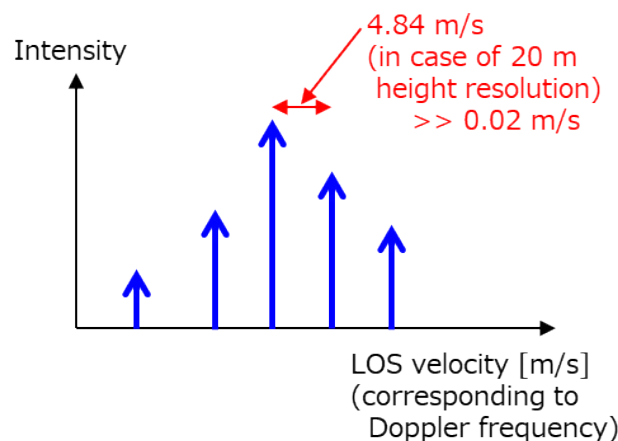


Fig. 11  Schematic of velocity bin of spectrum.

## 8. Comparison with past works

Here, the simulation procedure of this paper is compared with the past work which investigated the error in shear flow. The comparison is summarized in Table 7. While the procedure in the past works[18, 19] has used simplified numerical integration, this paper has employed the full Monte-Carlo simulation. Pulse shape is the only PCDL parameter which has been considered in the past works[18, 19]. This means the error which has been investigated in the past works[18, 19] was only $\Delta_C$. The influences of SNR profile and A/D conversion have been considered only in this paper. Consideration of these factors can be possible also for the past works[18, 19] by modifying the equation. However, the influences of the speckle noise, detector noise, spectral accumulation, and estimation algorithm can be considered exactly only in this paper. The weak point for the procedure of this paper is the time consumption. The simplified method of the past works[18, 19] is suitable to know rough tendency of influences regarding shear condition and PCDL performance.

Table 7　Comparison between simplified numerical integration and full Monte-Carlo simulation.
（○ : considered, × : not considered）

| Terms | | Simplified numerical integration (eqs. (9) and (10) in [18], eq. (4) in [19]) | Full Monte-Carlo simulation (this paper) |
|---|---|---|---|
| PCDL performance | Pulse shape | ○*1 | ○ |
| | SNR profile | ×*2 | ○ |
| | Speckle noise | × | ○ |
| | Detector noise | × | ○ |
| | A/D conversion | ×*2 | ○ |
| | Spectral accumulation | × | ○ |
| | Estimation algorithm | × | ○ |
| Calculation time | | Short | Time consuming |

*1 Triangle pulse shape has been employed in eq. (10) in [18] but can be replaces by more realistic shape.
*2 These factors can be considered in eq. (9) in [18] by using convolution and discretization which correspond to consideration of SNR and digitization.

## 9. Conclusions

Full-parameter performance simulation theory was shown for VAD-PCDL. Example analysis of wind speed measurement error is shown for the case of sheared wind flow. Some cases of the vertical wind profiles with shear were set for the input, and wind speed measurements using VAD scan were simulated using the FFT based signal processing. The larger receiving aperture diameter and the lower beam focusing height realize higher SNR at the beam focusing height and contributes to high data availability. However, these situations caused steeper SNR weighting around the beam focusing height. The errors caused by SNR weighting and/or height sensing error became larger for these cases while the shear curvature was not so distinct compared with other error sources. The errors regarding SNR weighting and height sensing error were more than ＋1% in some cases, and this error cannot be ignored in wind resource assessments if the NORSEWInD standard is referred. The simulation theory and results of this paper can clarify the source of errors in VAD-PCDL measurement. This clarification contributes to the optimized parameter design of VAD-PCDL (especially, the receiving aperture diameter and the beam focusing height), by considering requirements regarding horizontal wind speed measurement accuracy and data availability in wind resource assessment for wind energy application.

Although the wind field of this paper is limited in a simple case (i.e., horizontal shear with power law), the above-mentioned tendency on measurement error can be the basis of understanding for general wind field cases. The detector noise was neglected in the concrete simulation. However, this influence can be considered simply by using the noise term in eq. (5). Although the simulation in this study is limited for the case of a flat terrain, this can be modified for the measurement in a complex terrain by using the complex wind flow as an input. The application to the floating

VAD-PCDL systems for the offshore wind resource assessment is also possible, by combining with the motion of the buoy and the motion compensation algorithm. The scope of this paper has been limited in pulsed CDLs even though continuous-waves CDLs (CCDLs) have been also used in wind resource assessments[10, 11, 14]. Ranging in a CCDL is performed by utilizing the beam focusing effect, therefore, error caused by SNR weighting should be considered more carefully.

## Acknowledgement

## References

1) R. M. Huffaker and R. M. Hardesty, "Remote sensing of atmospheric wind velocities using solid-state and CO2 coherent laser systems," Proc. IEEE, **84**(2), 181−204 (1996).

2) J. M. Vaughan, K. O. Steinvall, C. Werner, and P. H. Flamant, "Coherent laser radar in Europe," Proc. IEEE, **84**(2), 205−226 (1996).

3) C. J. Karlsson, F. Å. A. Olsson, D. Letalick, and M. Harris, "All-fiber multifunction continuous wave coherent laser radar at 1.55 μm for range, speed, vibration, and wind measurement," Applied Optics, **39**(21), 3716−3726 (2000).

4) G. N. Pearson, R. J. Roberts, J. R. Eacock, and M. Harris, "Analysis of the performance of a coherent pulsed fiber lidar for aerosol backscatter applications," Applied Optics, **41**(30), 6442−6450 (2002).

5) J. P. Cariou, B. Augere, and M. Valla, "Laser source requirements for coherent lidars based on fiber technology," Comptes Rendus Physique, **7**(2), 213−223 (2006).

6) S. Kameyama, T. Ando, K. Asaka, Y. Hirano, and S. Wadaka, "Compact all-fiber pulsed coherent Doppler lidar system for wind sensing," Applied Optics, **46**(11), 1953−1962 (2007).

7) T. Ando, S. Kameyama, and Y. Hirano, "All-fiber coherent Doppler lidar technologies at Mitsubishi Electric Corporation," IOP Conference Series: Earth and Environmental Science, **1**, 012011 (2008).

8) M. Courtney, R. Wagner, and P. Lindelöw, "Testing and comparison of lidars for profile and turbulence measurements in wind energy," IOP Conference Series: Earth and Environmental Science, **1**, 012021 (2008).

9) N. Kotake, H. Sakamaki, M. Imaki, Y. Miwa, T. Ando, Y. Yabugaki, M. Enjo, and S. Kameyama, "Intelligent and compact coherent Doppler lidar with fiber-based configuration for robust wind sensing in various atmospheric and environmental conditions," Optics Express, **30**(11), 20038−20062 (2022).

10) D. A. Smith, M. Harris, A. S. Coffey, T. Mikkelsen, H. E. Jørgensen, J. Mann, and R. Danielian, "Wind lidar evaluation at the Danish wind test site in Høvsøre," Wind Energy, **9**(1−2), 87−93 (2006).

11) C. B. Hasager, A. Peña, M. B. Christiansen, P. Astrup, M. Nielsen, F. Monaldo, D. Thompson, and P. Nielsen, "Remote sensing observation used in offshore wind energy," IEEE Journal of Selected Topics in Applied Earth Observations and Remote Sensing, **1**(1), 67−79 (2008).

12) A. Clifton, P. Clive, J. Gottschall, D. Schlipf, E. Simley, L. Simmons, D. Stein, D. Trabucchi, N. Vasiljevic, and I. Würth, "IEA Wind Task 32: Wind lidar identifying and mitigating barriers to the adoption of wind lidar," Remote Sensing, **10**(3), 406 (2018).

13) J. Gottschall, B. Gribben, D. Stein, and I. Würth, "Floating lidar as an advanced offshore wind speed measurement technique: current technology status and gap analysis in regard to full maturity," Wiley Interdisciplinary Reviews: Energy and Environment, **6**(5), e250 (2017).

14) C. B. Hasager, D. Stein, M. Courtney, A. Peña, T. Mikkelsen, M. Stickland, and A. Oldroyd, "Hub height ocean winds over the North Sea observed by the NORSEWInD lidar array: measuring techniques, quality control and data management," Remote Sensing, **5**(9), 4280−4303 (2013).

15) S. Nabi, N. Nishio, P. Grover, R. Matai, Y. Kajiyama, N. Kotake, S. Kameyama, W. Yoshiki, and M. Iida, "Improving LiDAR performance in complex terrain using CFD-based correction and direct-adjoint-loop optimization," Journal of Physics Conference Series, **1452**(1), 012082 (2020).

16) IEA WIND Recommended Practices 15, "Ground-based vertically-profiling remote sensing for wind resource assessment," First Edition, (2013).

17) IEA WIND Recommended Practices 18, "Floating lidar systems," First Edition, (2017).

18) M. Courtney, A. Sathe, and N. G. Nygaard, "Shear and turbulence effects on lidar measurements," DTU Wind Energy, (E-0061), (2004).

19) J. K. Lundquist, M. J. Churchfield, S. Lee, and A. Clifton, "Quantifying error of lidar and sodar Doppler beam swinging mea-

surements of wind turbine wakes using computational fluid dynamics," Atmospheric Measurement Techniques, **8**(2), 907–920 (2015).

20) D. Zrnic, "Estimation of spectral moments for weather echoes," IEEE Transactions on Geoscience Electronics, **GE-17**(4), 113–128 (1979).

21) R. Frehlich, "Effects of wind turbulence on coherent Doppler lidar performance," Journal of Atmospheric and Oceanic Technology, **14**(1), 54–75 (1997).

22) S. Kameyama, T. Ando, K. Asaka, Y. Hirano, and S. Wadaka, "Performance of discrete-Fourier-transform-based velocity estimators for a wind-sensing coherent Doppler lidar system in the Kolmogorov turbulence regime," IEEE Transactions on Geoscience and Remote Sensing, **47**(10), 3560–3569 (2009).

23) R. G. Frehlich and M. J. Kavaya, "Coherent laser radar performance for general atmospheric refractive turbulence," Applied Optics, **30**(36), 5325–5352 (1991).

24) S. Kameyama, T. Ando, K. Asaka, and Y. Hirano, "Semianalytic pulsed coherent laser radar equation for coaxial and aperture systems using nearest Gaussian approximation," Applied Optics, **49**(27), 5169–5174 (2010).

25) R. Wagner, M. Courtney, J. Gottschall, and M. P. Lindelöw, "Accounting for the speed shear in wind turbine power performance measurement," Wind Energy, **14**(8), 993–1004 (2011).

26) R. Wagner, I. Antoniou, S. M. Pedersen, M. S. Courtney, and H. E. Jørgensen, "The influence of the wind speed profile on wind turbine performance measurements," Wind Energy, **12**(4), 348–362 (2009).

27) L. Fan, G. Qi, J. Xing, J. Jin, J. Liu, and Z. Wang, "Accurate frequency estimator of sinusoid based on interpolation of FFT and DTFT," IEEE Access, **8**, 44373–44380 (2020).

## Author introduction

Shumpei Kameyama received his M.E. degree from Keio University in 1995 and D.E. degree from Chiba University in 2011. Since 1995, he has been with Mitsubishi Electric Corporation, and he started the development of laser remote sensing systems in 1999. His current research involves coherent Doppler lidar, differential absorption lidar, and range imaging laser sensor. He is a member of IEEE, Optica, Japan Society of Applied Physics, and Laser Radar Society of Japan. He has received Technology Award from Japan Society for Aeronautical and Space Science, Technology Management Innovation Award from Japan Techno-Economics Society, and Significant Contributor Award from RTCA. He has elevated to IEEE Fellow in 2024.